ELSEVIER

#### Contents lists available at ScienceDirect

# Metabolism

journal homepage: www.journals.elsevier.com/metabolism





# Inhibition of microglial Slc2a5 attenuates ischemic brain injury

Daosheng Ai <sup>a,b,1</sup>, Baoshan Qiu <sup>b,c,1</sup>, Xing-jun Chen <sup>a,b,1</sup>, Fengzhi Li <sup>b,d,1</sup>, Di Yao <sup>b,f</sup>, Huijie Mi <sup>a,b</sup>, Jun-Liszt Li <sup>a,b</sup>, Bing Zhou <sup>e</sup>, Jian Zuo <sup>g</sup>, Yilong Wang <sup>b,c,\*</sup>, Woo-ping Ge <sup>b,h,i,\*</sup>, Wenzhi Sun <sup>b,f,\*</sup>

- <sup>a</sup> Academy for Advanced Interdisciplinary Studies (AAIS), Peking University, Beijing 100871, China
- <sup>b</sup> Chinese Institute for Brain Research, Beijing, Beijing 102206, China
- <sup>c</sup> Department of Neurology, Beijing Tiantan Hospital, Capital Medical University, Beijing 100071, China
- d State Key Laboratory of Cognitive Neuroscience and Learning, Beijing Normal University, Beijing 100875, China
- <sup>e</sup> School of Engineering Medicine, Beihang University, Beijing 100191, China
- f School of Basic Medical Sciences, Capital Medical University, Beijing 100069, China
- <sup>8</sup> Ting Therapeutics, Inc., 6868 Nancy Ridge Dr., San Diego, CA 92121, USA.
- h Beijing Institute for Brain Research, Chinese Academy of Medical Sciences & Peking Union Medical College, Beijing 102206, China
- i Changping Laboratory, Beijing, 102206, China

#### ARTICLE INFO

#### Keywords: Microglia Slc2a5 Acute ischemic stroke

#### ABSTRACT

Acute ischemic stroke (AIS) is one of the leading causes of mortality and disability globally. Despite its complex pathological mechanisms, effective neuroprotective strategies are still lacking in clinical practice. Microglia and their metabolic processes play a pivotal role in the pathogenesis of AIS, yet the impact and underlying mechanisms of microglial fructose metabolism remain unclear. In this study, we identified \$\$Ic2a5\$ (also known as \$\$Glut5\$), a crucial regulator of fructose metabolism in microglia, as a key factor contributing to the early progression of AIS. Conditional deletion of \$\$Slc2a5\$ in microglia significantly alleviated brain injury in a mouse model of AIS. Single-cell transcriptomic (scRNA-seq) analysis demonstrated that the deletion of \$\$Slc2a5\$ promoted the differentiation of microglia into stroke-associated subpopulations with neuroprotective properties. Moreover, in vitro experiments indicated that this microglial differentiation process was primarily mediated by the activity of pyruvate kinase M2 (PKM2). Collectively, our findings unveil a novel microglial \$\$Slc2a5\$-mediated fructose metabolism pathway that exacerbates brain injury after AIS. This study provides evidence for \$\$Ic2A5\$ as a promising therapeutic target for the clinical treatment of AIS by offering insights into its critical role in microglial metabolism and neuroprotection.

### 1. Introduction

AIS persists as one of the leading causes of global mortality and long-term disability, imposing a substantial epidemiological and socioeconomic burden on healthcare systems worldwide [1]. According to the Global Burden of Disease (GBD) Study, stroke affected approximately 12 million people and caused about 6.6 million deaths worldwide in 2019, with ischemic stroke accounting for roughly two-thirds of all cases [2]. Demographic shifts toward aging populations and modifiable risk factors, including sedentary lifestyles, further amplify the rising incidence of AIS [3]. Although modern thrombolysis and endovascular restore flow [4], no drug has achieved durable neuroprotection, making the

molecular dissection of AIS an urgent priority for next-generation therapy.

Mounting evidence implicates neuroinflammation as a central mediator of AIS progression [5]. Following ischemic injury, microglia, the resident immune cells of the central nervous system (CNS), are rapidly activated, playing a key role in initiating and amplifying inflammatory responses [6]. These cells exhibit a dualistic role: proinflammatory polarization exacerbates neuronal death through cytokine/chemokine release (e.g., IL-1 $\beta$ , TNF- $\alpha$ ), while anti-inflammatory phenotypes promote tissue repair via phagocytic clearance of cellular debris [7]. Notably, Colony Stimulating Factor 1 Receptor (CSF1R) antagonist-mediated microglial depletion in murine stroke models

<sup>\*</sup> Corresponding authors at: Chinese Institute for Brain Research, Beijing, Beijing 102206, China. E-mail addresses: yilong528@aliyun.com (Y. Wang), woopingge@cibr.ac.cn (W.-p. Ge), sunwenzhi@cibr.ac.cn (W. Sun).

<sup>&</sup>lt;sup>1</sup> These authors contributed equally to this work.

increases infarct volume and neuronal loss, unequivocally demonstrating their essential protective functions [8]. Emerging evidence further implicates microglial metabolic plasticity as a determinant of functional polarization. For instance, hexokinase 2 (HK2)-dependent glycolysis governs microglial activation, with *Hk2* ablation worsening post-stroke neuroinflammation and injury [9]. Recent studies have demonstrated that the metabolic state of microglia directly influences their functional phenotype, with metabolic reprogramming determining whether they promote neuroinflammation or exert neuroprotective effects after stroke [10]. However, the underlying mechanisms linking microglial metabolism and functional regulation in ischemic stroke remain poorly understood.

Epidemiological and preclinical studies highlight dietary fructose as a modifiable risk factor for AIS [11]. High-fructose diets (HFD), prevalent in modern processed foods, are mechanistically linked to systemic metabolic dysregulation, including insulin resistance and chronic inflammation [12–14]. However, their role in ischemic stroke remains poorly understood. Emerging evidence suggests that HFD not only exacerbates systemic inflammation but may also influence CNS metabolic pathways, potentially worsening stroke outcomes [11]. For example, HFD has been shown to alter CNS energy metabolism, promote oxidative stress, and enhance neuroinflammation, all of which are critical factors contributing to ischemic brain injury [15].

Within the CNS, fructose uptake is predominantly mediated by SLC2A5, a transporter that is highly enriched in microglia [16,17]. It remains untested whether systemic signals modulate this uptake; here we focus on its cell-autonomous role in stroke. Despite these associations, the causal role of microglial fructose metabolism in AIS—and its potential as a therapeutic target—remains unexplored.

Accordingly, this study sets out to determine whether microglial Slc2a5 acts as the key metabolic sensor that converts excess dietary fructose into heightened acute ischemic stroke injury. Using a conditional Slc2a5 knockout mouse maintained on a high-fructose diet, we dissect how fructose uptake governs microglial phenotype and whether blocking this single transporter—thereby interrupting downstream PKM2 activity—can reprogram microglia toward a neuroprotective state and, ultimately, lessen stroke severity.

#### 2. Methods

# 2.1. Experimental animals and genotyping

Animal use and care adhered to the guidelines established by the Chinese Institute for Brain Research's Institutional Animal Care and Use Committee, Beijing.  $Slc2a5^{-/-}$  mice [18] were provided by the laboratory of Professor Zuo Jian from St. Jude Children's Research Hospital, USA. Tmem119-creER [19] (No.031820) and Cx3cr1-EGFP (No.005582) mice were obtained from Jackson Laboratory. The  $Slc2a5^{fl/fl}$  mouse line (C57BL/6 background) was designed and generated in Woo-ping Ge's laboratory with assistance from Biocytogen Pharmaceuticals. C57BL/6 control mice were acquired from Charles River Laboratories.

Tail biopsies were taken at P14 and genomic DNA was extracted using a standard alkaline lysis or a commercial kit (e.g., QuickExtract). Genotyping PCR was performed to detect the presence of the targeted sequences. PCR cycling conditions: initial denaturation at 95 °C for 3 min; 35 cycles of 95 °C for 30 s, 58–62 °C for 30 s, 72 °C for 45 s; final extension at 72 °C for 5 min. PCR products were resolved on a 1.5 % agarose gel and visualized with GelRed/EtBr. Genotyping calls were made by two independent experimenters.

Tamoxifen (T5648, Sigma) was dissolved in absolute ethanol and corn oil (1:9) at 10 mg/ml by shaking at 37  $^{\circ}$ C overnight, aliquoted and stored at -20  $^{\circ}$ C. Adult male mice (25–30 g; 8–12 weeks) received tamoxifen 100 mg/kg i.p. once daily for 5 consecutive days. Unless otherwise specified, mice were allowed a 14-day recovery/washout period after the final tamoxifen injection before any terminal procedures or experiments to allow full recombination and clearance of tamoxifen.

#### 2.2. High fructose diet treatment

In this study, two purified diets provided by Jiangsu Xietong Pharmaceutical Bio-Engineering Co., Ltd. (abbreviated as Xietong Shengwu) were utilized. For the high fructose diet (HFD) experiments, the control group (D24508) and the high-fructose group (D02022704), containing 60 % fructose, were employed. The mice were fasted for 24 h and then fed the purified diet for one month prior to the experiment.

#### 2.3. Transient middle cerebral artery occlusion (tMCAO) model

Ischemic stroke was induced via tMCAO as described in the reference [20]. In brief, male mice weighing 25–30 g were anesthetized with isoflurane (4–5 % for induction, 1–2 % for maintenance). After disinfection and a midline incision of the neck skin, the common carotid artery and external carotid artery were exposed and tied off using silk sutures. Subsequently, a heparin-coated filament (602356PK5Re, Doccol) was gently inserted into the origin of the middle cerebral artery through an incision in the common carotid artery. If drug treatment was required, the mice were injected into the fundus vein at this time. After 60 min of occlusion, the filament was carefully removed, and blood flow was assessed using a laser speckle contrast imaging system (Simopto, Wuhan XunWei Optoelectronic Technology Co., Ltd., China). Mice were allowed to recover in a warm chamber and then transferred to cages containing gel with sterilized water after the operation.

#### 2.4. mNSS score and 2, 3, 5-triphenyltetrazolium chloride (TTC) staining

Neurological function was assessed 24 h after tMCAO by an observer who was unaware of the genotype of the mice using a scoring system derived from a previous study [21]. After the neurological assessment, the brain was centrally cut into six 1-mm continuous coronal sections with a fixed reabrasive. Sections were stained with 2 % TTC in PBS at 37 °C for 5 min and then fixed in 4 % paraformaldehyde (PFA) for 12 h. TTC-stained sections were scanned and digitized. The area of the TTC negative area and the ipsilateral hemisphere was measured using ImageJ software. The percentage of cerebral infarction volume was calculated using the following formula: (sum of cerebral infarction area / sum of brain slice area) multiplied by a scaling factor, which is the area of the contralateral hemisphere divided by the area of the ipsilateral hemisphere, derived from an edema correction method [22].

# 2.5. Immunostaining

Mouse brains were processed for whole-mount staining as previously reported [23]. Mice were perfused with 50 ml of 0.1 mol/L PBS, followed by 30 ml of 4 % PFA (in PBS). The brains were then fixed in 4 % PFA for 24 h at 4 °C, washed in PBS for 30 min, and transferred to 30 % sucrose. After 72 h, the brains were cut into 60 µm slices for staining. For immunostaining, slices were blocked with 0.3 % Triton X-100, 5 % normal donkey serum, and 1 % BSA in PBS for 1 h at 37 °C. Slices were then incubated with primary antibodies (e.g., IBA1) dissolved in PBS with 0.3 % Triton X-100 at 4  $^{\circ}$ C for 24–48 h. After washing three times in PBS for 10 min each, slices were incubated with secondary antibodies and Hoechst 33342 dissolved in PBS with 0.3 % Triton X-100 at 37  $^{\circ}\text{C}$  for 2 h. Antibodies used included anti-IBA1 (Abcam AB178846, 1:300) and anti-SPP1 (R&D Systems AF808, 1:300). Secondary antibodies included goat anti-rabbit IgG H&L Alexa Fluor 488 (A11008), goat anti-rabbit IgG H&L Alexa Fluor 546 (A11035), donkey anti-rabbit IgG H&L Alexa Fluor 647 (A31573), donkey anti-rat IgG H&L Alexa Fluor 488 (A21208), goat anti-rat IgG H&L Alexa Fluor 546 (A11081), goat anti-rat IgG H&L Alexa Fluor 647 (A21247), and donkey Anti-Goat IgG H&L Alexa Fluor 555 (ab150134), Donkey Anti-Goat IgG H&L Alexa Fluor 488 (ab150129), Donkey Anti-Goat IgG H&L Cy5 (ab6566), all used at a 1:500 dilution. Samples were mounted with Fluoro-Gel anti-fade mounting medium (Electron Microscopy Sciences Cat#17985-11) and imaged using a

Leica SP8 confocal microscope with either a  $20\times/0.75$  NA or  $40\times/1.30$  NA objective and Leica Application Suite software.

#### 2.6. Microglia isolation

Mice at an age of postnatal day (P)30-45 were anesthetized with isoflurane. They were perfused transcardially with ice-cold PBS (Corning). Brains were isolated and immediately immersed into cold hibernation medium (5 mM KCl, 5 mM NaOH, 5 mM NaH2PO4, 0.5 mM MgCl<sub>2</sub>, 20 mM Sodium pyruvate, 5.5 mM Glucose, 200 mM Sorbitol, pH 7.2-7.4, filtered with  $0.22 \, \mu m$  filters). Dissected brain hemispheres were cut into small pieces and incubated in cold hibernation medium (BrainBits, USA) containing papain (2 mg/ml, Sigma) and DNase I (100 units, Sigma) at 37 °C for 30 min with intermittent flicking. The tissue was triturated into individual cell suspension by a siliconized Pasteur pipette with a fire-polished tip (BrainBits). Cell suspensions were added to an Optiprep gradient (Brewer and Torricelli, 2007b) and centrifuged at 900g for 15 min at 4  $^{\circ}$ C. We then removed most of the upper 5 ml of debris and collected specific Optiprep layers (neurons and astrocytes were enriched in upper layers while microglia were enriched in pellets). Cells from different layers were washed with cold hibernation medium without Ca<sup>2+</sup> and Mg<sup>2+</sup> (BrainBits) and centrifuged at 600g for 10 min at 4 °C. Cell pellets were resuspended in 500  $\mu$ l of cold hibernation medium for sorting.

#### 2.7. Cell culture

BV2 cells (the vector center was purchased from Shanghai Enzhuan Biotechnology Co., Ltd.), were cultured in DMEM high-glucose medium (Gibco, 11965092) and supplemented with 10 % fetal bovine serum (Gibco, 10091148). Transfection was performed when the cell density reached 70 %. The sgRNA design for the *Slc2a5* gene was obtained from the GPP sgRNA designer. Two sgRNAs were obtained:

sgRNA1: CCGGATACGAGCTGAAGT; sgRNA2: TGACGCTGCTGTGGTCCTCG.

These two sgRNAs were synthesized by GenScript and combined with plasmids using T4 ligase respectively. Each sgRNA was ligated to one plasmid. To ensure the knockout efficiency of the gene, two plasmids carrying different sgRNAs were transfected into BV2 cells together using jetOPTIMUS® DNA Transfection Reagent (Polyplus-transfection, 101000006). After 24 h of expression, monoclonal cells were selected by flow cytometry.

The monoclonal cells from the above experiment were collected. 100  $\mu l$  of cell lysis buffer (NOVAZON, PD101–01) was added to lyse the DNA of the cells. The PCR amplification products were amplified using the following conditions: 98 °C for 3 min; 34 cycles of 98 °C for 10 s, 63.8 °C for 10 s, and 72 °C for 1 min; 72 °C for 5 min. The PCR amplification products were sent to RiboScience for sequencing to detect the knockout situation of Slc2a5.

# 2.8. PKM2 drugs experiment

BV2 cells were cultured in 24-well culture plates with coverslips. PKM2 treatment with C3k (MCE, HY-103617) or TEEP-46 (MCE, HY-103617) was also performed. First, the cells were grown in DMEM medium containing 10 % FBS, and when the cell density reached 65 %, the medium was discarded and washed twice with PBS. Then, cultures were grown using DMEM (glucose-free) (Gibco, 11966025) medium supplemented with 10 % fetal bovine serum and 3 mM fructose. Meanwhile, BV2 cells were incubated with the PKM2 drug for 24 h. After 24 h, the medium was discarded and rinsed twice with PBS. Finally, the medium was changed to sugar-free DMEM medium containing the PKM2 drug for 6 h of OGD experiments in the absence of oxygen.

#### 2.9. Western blot analysis

The protocol was based on the previous study [24]. BV2 cells from different experimental groups were harvested in RIPA buffer (P0013B, Biyotime). The proteins from each group were electrophoresed using precast gel (MA0449–1, MeilunGel) and subsequently transferred to membranes. After blocking the membranes with 5 % milk, antibodies against SLC2A5 (1:500 , MA1-036×, Thermo Scientific) and  $\beta$ -actin (1:5000, 66009–1-Ig, ProteinTech Group Inc.) were added and incubated overnight at 4 °C. Following this, the membranes were incubated with a secondary antibody (1:15,000, ZB-2305, ZSGB-BIO) for 1 h at room temperature in the dark. Gel images were captured and quantified using a chemiluminescence imaging system (Minichemi-610). Relative densitometric values were calculated after normalization to  $\beta$ -actin.

#### 2.10. Bulk RNA sequencing and analysis

Total RNA was extracted from microglia using an RNeasy Micro Kit (Qiagen, 74004) following the manufacturer's protocol. The DNA library for sequencing was prepared following the protocol for the SMARTer Stranded Total RNA-Seq Kit v2. RNA sequencing was performed with an MGI 2000 sequencer under a 100-bp paired-end sequencing strategy. At least 6G of sequencing depth was obtained for each sample. RNA-seq raw data were initially filtered with "FastQC" to obtain clean data after quality control. Clean data were aligned to the reference genome (Version: GRCm38) downloaded from GENCODE by HISAT2 [25]. Raw counts for each gene were calculated by FeatureCounts [26]. The expression level of detected genes was estimated by DESeq2 (version 1.36.0) [27]. A volcano plot was generated by ggplot2 (version 3.4.2) in R (version 4.2.1), with a cutoff of adjusted *p*-value <0.01 and the absolute value of log<sub>2</sub> (Fold change) > 1, measured by DESeq2. The heat map was generated by the heatmap function with the z-score of each gene. GSEA was performed using the ClusterProfiler (version 4.4.4) package in R, with an adjusted p-value < 0.05 [28].

#### 2.11. Cell preparation

After harvesting, tissues were washed in ice-cold RPMI 1640 and dissociated using the Multi-tissue dissociation kit 2 (Miltenyi Catalog No.130–110-204) from Miltenyi Biotec as instructions. DNase treatment was optional according to the viscosity of the homogenate. Cell count and viability were estimated using a fluorescence cell analyzer (Count-star® Rigel S2) with AO/PI reagent after the removal of erythrocytes (Miltenyi Catalog No.130–094-183) and then the removal of debris and dead cells was decided to be performed or not (Miltenyi Catalog No.130–109-398/130–090-101). Finally, fresh cells were washed twice in RPMI 1640 and then resuspended at  $1\times10^6$  cells per ml in  $1\times$  PBS and 0.04 % bovine serum albumin.

#### 2.12. Single cell RNA sequencing

Single-cell RNA-Seq libraries were prepared using the SeekOne® MM Single Cell 3' library preparation kit (SeekGene Catalog No.SO01V3.1). Briefly, an appropriate number of cells were loaded into the flow channel of SeekOne® MM chip, which had 170,000 microwells, and allowed to settle in microwells by gravity. After removing the unsettled cells, sufficient Cell Barcoded Magnetic Beads (CBBs) were pipetted into the flow channel and also allowed to settle in microwells with the help of a magnetic field.

Next, excess CBBs were rinsed out and cells in the MM chip were lysed to release RNA which was captured by the CBB in the same microwell. Then, all CBBs were collected, and reverse transcription was performed at 37 °C for 30 min to label cDNA with cell barcode on the beads. Further Exonuclease I treatment was performed to remove unused primer on CBBs. Subsequently, barcoded cDNA on the CBBs was hybridized with random primer, which had reads 2 SeqPrimer sequence

on the 5' end and could extend to form the second strand DNA with cell barcode on the 3' end. The resulting second strand DNA was denatured off the CBBs, purified, and amplified in PCR reaction. The amplified cDNA product was then cleaned to remove unwanted fragments and added to full-length sequencing adapter and sample index by indexed PCR. The indexed sequencing libraries were cleaned up with SPRI beads, quantified by quantitative PCR (KAPA Biosystems KK4824) and then sequenced on Illumine NovaSeq 6000 with PE150 read length or DNBSEQ-T7 platform with PE100 read length.

#### 2.13. Single nucleus RNA sequencing

Single nucleus RNA-Seq libraries were prepared using the SeekOne® Digital Droplet Single Cell 3' library preparation kit (SeekGene Catalog No.K00202). Briefly, an appropriate number of cells were mixed with reverse transcription reagent and then added to the sample well in the SeekOne® DD Chip S3. Subsequently, Barcoded Hydrogel Beads (BHBs) and partitioning oil were dispensed into the corresponding wells separately in chip S3. After emulsion droplet generation, reverse transcription was performed at 42  $^{\circ}$ C for 90 min and inactivated at 80  $^{\circ}$ C for 15 min. Next, cDNA was purified from the broken droplet and amplified in a PCR reaction. The amplified cDNA product was then cleaned, fragmented, end repaired, A-tailed and ligated to the sequencing adaptor. Finally, indexed PCR was performed to amplified the DNA representing 3' polyA part of expressing genes, which also contained Cell Barcode and Unique Molecular Index. The indexed sequencing libraries were cleaned up with SPRI beads, quantified by quantitative PCR (KAPA Biosystems KK4824) and then sequenced on the Illumina NovaSeq 6000 with PE150 read length.

# 2.14. ScRNA-seq or snRNA-seq downstream analysis

The downstream analysis was performed as previously reported [29]. Raw scRNA-seq reads underwent preprocessing using CellRanger (version 3.1.0) and were then aligned to the mouse reference genome (GRCm38 from UCSC) using the gene annotation file from GENCODE (mouse v32). The raw gene-by-barcode matrices generated by Cell Ranger were merged using AnnData in Python (version 3.12.9), following instructions in the SCANPY (version 1.11.1) tutorial. In the quality control step, we retained cells with a minimum gene count of 300 and a minimum cell count of 50 for the expression of the gene of interest. Cells with a mitochondrial proportion of 10 % or higher were filtered out. Subsequently, the count matrix was log-transformed [30].

Harmony (version 0.0.10) [31], with default parameters, was used for batch removal, and Louvain clustering was performed with a resolution parameter set to 1.0. For annotation of major cell types, manual evaluation of classic marker genes was used (endothelial cell, *Pecam1* and *Cldn5*; astrocyte, *Aqp4* and *Slc1a2*; macrophage, *Cd83* and *Cd163*; oligodendrocyte precursor cell, *Pdgfra*; excitatory neuron, *Gap43*, *Syn2* and *Slc17a6*; inhibitory neuron, *Gap43*, *Syn2* and *Gad1*; perivascular fibroblast, *Dcn* and *Col1a2*; microglia, *Tmem119* and *Gpr43*; oligodendrocyte, *Mbp* and *Mobp*; choroid plexus epithelial cell, *Sostdc1*). A Wilcoxon test with tie correction was used to obtain ranked marker genes. Gene set enrichment analysis was performed using GSEAPY [32]. *Cell-Chat* (version 2.1.2) was used for cell–cell communication analyses, following their recommended tutorials [33].

#### 2.15. Statistics and reproducibility

All the quantified data were analyzed using *GraphPad Prism* (version 9.0). A two-tailed unpaired Student's t-test was used to evaluate the difference between two groups, and the mean  $\pm$  SEM is presented with the individual data points shown simultaneously. Statistical significance was analyzed by p-value (\*p < 0.05, \*\*p < 0.01, \*\*\*p < 0.001). The independent repeated data for each experiment are described in the corresponding figure legend.

#### 3. Results

#### 3.1. Slc2a5 deficiency mitigates ischemic stroke-induced brain injury

Chronic fructose exposure exacerbates cerebrovascular injury in murine models of AIS [34]. To elucidate the causal relationship between dietary fructose intake and post-ischemic outcomes, we implemented a controlled dietary intervention paradigm (Fig. 1a). Quantitative assessment with an edema correction method [22] of cerebral infarct volumes 24 h after AIS, using standard TTC staining, revealed significant diet-dependent effects (Fig. 1b). HFD-fed mice demonstrated significantly increased cerebral infarct volumes compared to normodietary controls (Fig. 1c). Pharmacological inhibition of SLC2A5 using 2,5anhydro-D-mannitol (2,5-AM; 200 mg/kg) significantly attenuated infarct volumes versus vehicle-treated HFD cohorts (Fig. 1c), establishing Slc2a5 as a critical mediator of fructose-aggravated ischemic injury. Similarly, HFD-fed mice displayed markedly higher modified neurological severity scores (mNSS), reflecting more pronounced neurological deficits (Fig. 1d). Consistent with previous findings, these results confirm that prolonged fructose consumption aggravates brain injury following AIS. While 2,5-AM treatment effectively reduced infarct volumes, it did not result in a significant improvement in neurological function as measured by mNSS (Fig. 1d). To further evaluate the role of Slc2a5 in AIS, we used Slc2a5 knockout mice [18] and subjected them to tMCAO (Fig. 1e). Twenty-four hours post-AIS, Slc2a5 knockout mice exhibited significantly smaller infarct volumes and improved neurological function compared to wild-type controls (Fig. 1f-h). These results indicate that Slc2a5 deficiency markedly alleviates brain injury and enhances neurological recovery following AIS.

# 3.2. Microglial Slc2a5 deficiency alleviates ischemic stroke-induced brain injury

Previous studies have reported that *Slc2a5* is expressed in various cell types within the brain [35]. To accurately determine the expression pattern of *Slc2a5* across different brain cell types, we performed scRNA-seq on brain cortex from WT and Slc2a5-KO mice (Fig. 2a). Integration and clustering analysis of the samples, visualized using UMAP, identified 16 cell subpopulations comprising a total of 18,705 cells (Fig. 2b). Visualization and proportional analysis of cell subpopulations between the KO and WT groups revealed no significant differences in the number of microglial subpopulations (Fig. 2c, d).

Marker gene enrichment analysis for each subpopulation identified the MP subpopulation, characterized by high expression of *Pf4* and *Ms4a7* (Fig. 2e). Two distinct microglial subpopulations, both expressing *Cx3cr1* and *P2ry12*, were also identified (Fig. 2e). Notably, the MG\_1 subpopulation exhibited elevated expression of inflammation-related genes, including *Bcl2a1b* and *Il1a* (Fig. 2e). Interestingly, we observed specific high expression of *Slc2a5* within the microglial subpopulations (Fig. 2f and Extended Data Fig. 1a), suggesting that microglial *Slc2a5* may play a role in the progression of brain injury following AIS.

Meanwhile, we investigated the impact of whole-body *Slc2a5* knockout on gene expression across diverse neuronal subpopulations within the mouse cortex using gene set enrichment analysis (GSEA). Results revealed significant alterations in gene expression pathways across ten cortical cell subtypes following *Slc2a5* ablation (Extended Data Fig. 1b). Specifically, distinct effects were observed in two microglia subpopulations, manifested as differential enrichment of signaling pathways. MG\_2 exhibited enhanced oxidative phosphorylation, carbohydrate-activated cellular response, and adaptive thermogenesis pathways following *Slc2a5* knockout. Conversely, MG\_1 showed enhanced chemotaxis and cell migration pathways (Extended Data Fig. 1b). Intriguingly, both microglial subpopulations displayed suppressed cytoplasmic translation pathways. These findings illuminate the differential impact of whole-body *Slc2a5* knockout on gene expression pathways within distinct microglial subpopulations.

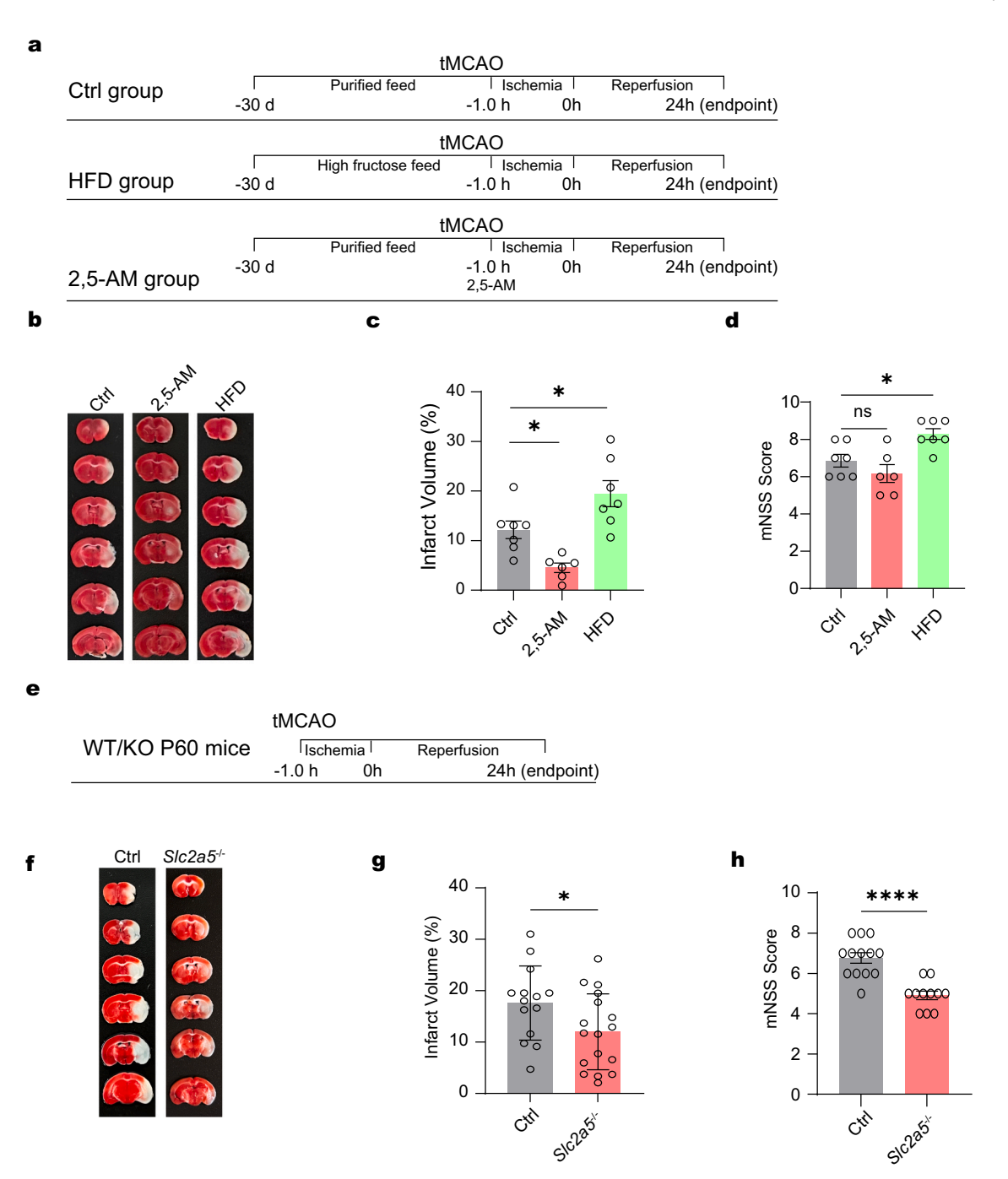
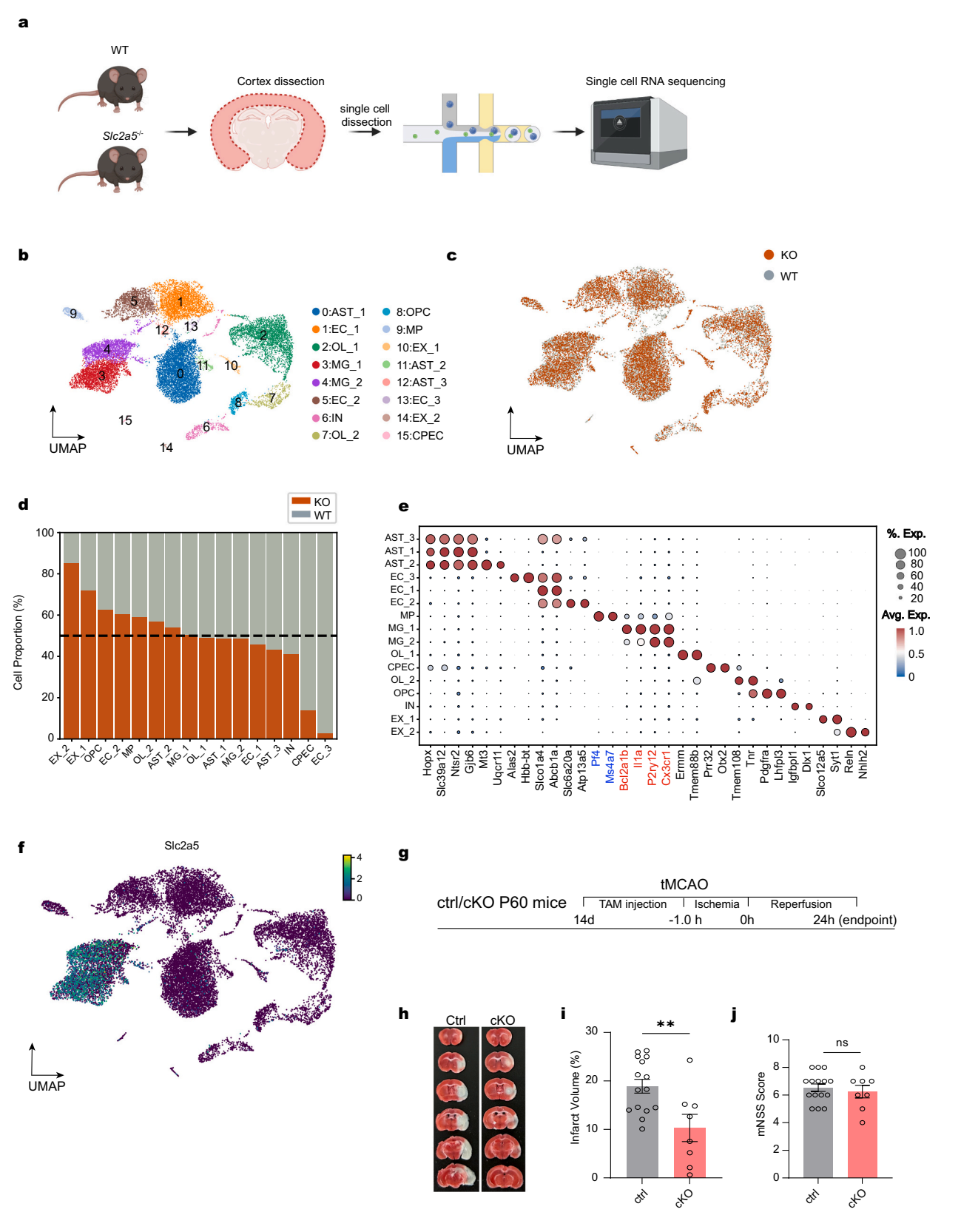


Fig. 1. Slc2a5 deficiency protects against acute ischemic stroke

- a. Schematic representation of the experimental design for tMCAO in the control (Ctrl), 2,5-AM, and high fructose diet (HFD) groups.
- b. Representative images of TTC staining from coronal brain sections at 24 h after ischemic stroke in the Ctrl, 2,5-AM, and HFD groups.
- c. Quantification of infarct volume reveals significant differences among the groups, with reduced infarct volume in the 2,5-AM (n=6) and HFD (n=7) compared to Ctrl (n=7) (overall p-value <0.001, \*p < 0.05). Data are presented as mean  $\pm$  SEM, with individual data points shown. Statistical significance was determined by one-way ANOVA followed by Dunnett's post-hoc testing.
- d. The modified Neurological Severity Score (mNSS), which assesses motor and sensory function, indicates significant differences, with 2,5-AM (n=6) and HFD (n=7) groups performing worse than Ctrl (n=7) (overall p-value <0.01, \*p<0.05). No significant difference (ns) was found between the 2,5-AM and HFD groups. Data are presented as mean  $\pm$  SEM, with individual data points shown. Statistical significance was determined by one-way ANOVA followed by Dunnett's post-hoc testing.
- e. Schematic representation of the experimental design for tMCAO in the Ctrl and Slc2a5<sup>-/-</sup> groups.
- f. Representative images of coronal brain sections from the Ctrl and *Slc2a5*<sup>-/-</sup> groups.
- g. Infarct volume shows significant differences, with  $Slc2a5^{-/-}$  (n = 17) exhibiting a greater volume compared to Ctrl (n = 14) (\*p < 0.05). Data are presented as mean  $\pm$  SEM, with individual data points shown. Statistical significance was determined by an unpaired t-test.
- h. mNSS analysis shows marked functional impairment in  $Slc2a5^{-/-}$  (n=11) compared to Ctrl (n=13) (\*\*\*\*p<0.0001). Data are presented as mean  $\pm$  SEM, with individual data points shown. Statistical significance was determined by an unpaired t-test.



(caption on next page)

Fig. 2. Slc2a5 deficiency in microglia protects against ischemic stroke

- a. Schematic representation of the single-cell transcriptome from the cortex of wild-type (WT) and  $Slc2a5^{-/-}$  mice.
- b. UMAP visualization of single-cell transcriptional profiles from the cortex of WT and Slc2a5<sup>-/-</sup> mice, colored by identified cell types, including astrocyte (AST), endothelial cell (EC), oligodendrocyte (OL), microglia (MG), inhibitory neuron (IN), oligodendrocyte precursor cell (OPC), excitatory neuron (EX), and choroid plexus epithelial cell (CPEC).
- c. Distribution of cells from Slc2a5<sup>-/-</sup> (KO, orange) and wild-type (WT, gray) across the UMAP, illustrating differences in cellular composition.
- d. Bar graph showing the proportion of cell types as a percentage, highlighting the reduced representation of certain populations in KO compared to WT.
- e. Dot plot representing the percentage of expression and average expression levels of marker genes across various cell types, emphasizing distinct expression patterns between KO and WT.
- f. UMAP visualization of Slc2a5 expression, indicating enriched regions in two groups of microglial states.
- g. Schematic representation of tMCAO in control (Ctrl) and Tmem119-creER::Slc2a5<sup>-/-</sup> (cKO) groups.
- h. Representative images of coronal brain sections from Ctrl and cKO display infarct regions.
- i. Quantification of infarct volume reveals a significant increase in cKO (n = 8) compared to Ctrl (n = 15) (\*\*p < 0.01). Statistical significance was determined using an unpaired t-test.
- j. Modified Neurological Severity Score (mNSS) shows no significant difference (ns) between Ctrl (n = 15) and cKO (n = 8). Data are presented as mean  $\pm$  SEM, with individual data points shown. Statistical significance was determined using an unpaired t-test.

To further investigate the impact of systemic Slc2a5 knockout on microglia interactions with other cells, we used CellChat to perform differential cell-cell communication (CCC) analysis on two scRNA-seq datasets, identifying the cellular signaling pathways through which microglia influence other cell populations post systemic Slc2a5 knockout [33]. Initially, by analyzing intercellular communication differences among microglial subpopulations, our results revealed differential signaling pathway activity in two microglial subpopulations following systemic Slc2a5 knockout. In MG 1, the CSF signaling pathway was suppressed, while in MG\_2, the PROS signaling pathway was suppressed, and the TNF pathway was enhanced (Extended Data Fig. 1c). Visualization of the expression of genes related to these three pathways across subpopulations revealed that systemic Slc2a5 knockout led to suppressed Tnfrsf1b expression in both MG 1 and MG 2 (Extended Data Fig. 1d). To further assess the impact of microglial subpopulations on receptor-ligand pairs within the signaling pathways of other subpopulations, we found that the TNF-TNFRSF1B signaling pathway in MG\_1 and MG\_2 was suppressed in Slc2a5 knockout (Extended Data Fig. 1e-h). A previous study has shown that microglial *Tnfrsf1b* knockout reduces brain lesion size following acute CNS injury [36], suggesting that the ablation of microglial Slc2a5 exhibits neuroprotective effects under physiological conditions.

To investigate this further, we generated *Tmem119-CreER*::*Slc2a5*<sup>fl/fl</sup> mice to achieve microglial deletion of *Slc2a5* and subjected these mice to the tMCAO model (Fig. 2g). TTC staining revealed that the infarct volume at 24 h post-stroke was significantly smaller in conditional knockout (cKO) mice compared to WT controls (Fig. 2h, i). These results indicate that microglial *Slc2a5* deletion mitigates brain injury following AIS. However, no significant differences in neurological function scores were observed between cKO and WT mice at 24 h post-stroke (Fig. 2j).

# 3.3. Slc2a5 deficiency promotes the differentiation of stroke-associated microglia in ischemic stroke

To further investigate the role of *Slc2a5* in microglia-mediated brain injury following AIS, we generated four experimental groups: Slc2a5-KO\_control, Slc2a5-KO\_stroke, WT\_control, and WT\_stroke. Brain tissues were collected 24 h post-stroke for single-nucleus RNA sequencing (snRNA-seq) (Fig. 3a). After integrating data from all four groups, we identified 19 distinct cell subpopulations comprising a total of 44,675 cells (Fig. 3b). This study further quantified the distribution of these cell subpopulations in the infarct and non-infarct areas of both the knockout and control groups (Extended Data Fig. 2a, b). Results revealed a greater number of neurons and fewer non-neuronal cells in the infarct area of the *Slc2a5* knockout group compared to the wild-type group, suggesting enhanced neuronal survival within the infarct region following *Slc2a5* ablation (Extended Data Fig. 2c). Since *Slc2a5* is specifically expressed in microglia, we isolated microglia from these datasets, obtaining a total of 1515 cells, which were classified into four microglial cell

subpopulations through dimensionality reduction and cluster analysis (Extended Data Fig. 2e). Microglial subpopulation 0 exhibited significantly higher expression of the homeostatic marker gene Tmem119 (Extended Data Fig. 2f). Comparison of the proportions of these four subpopulations in infarct versus non-infarct regions within both Slc2a5 knockout and control groups (Extended Data Fig. 2g), revealed that subpopulations 0, 2, and 3 were less prevalent in infarct areas than in non-infarct areas in both groups. Given the high Tmem119 expression in subpopulation 0, this suggests it is homeostatic-associated microglia (HAM). Conversely, subpopulation 1 showed significantly higher prevalence in infarct areas than in non-infarct areas in both Slc2a5 knockout and control groups, indicating its association with stroke-associated microglia (SAM). Consequently, only 1315 HAM and SAM cells were isolated for downstream analysis (Fig. 3c). Within the microglia, two subpopulations were defined, and their proportions across the four groups were analyzed. We found that SAM were derived from HAM by RNA velocity trajectory analysis (Fig. 3c).

Marker gene enrichment analysis revealed that Spp1, Adam8, and Ccl4 were specifically expressed in SAM (Fig. 3d). GSEA of the two microglial subpopulations showed significant enrichment of oxygenresponse pathways in SAM and complement activation pathways in HAM (Fig. 3e). To identify the driver genes promoting the differentiation of HAM to SAM in these two microglial subpopulations, we utilized scVelo analysis and revealed Spp1, Lingo2, and Ncam2 as key drivers of this transition (Fig. 3f) [37]. To investigate the transcription factors influencing SAM driver gene expression, this study employed decoupled analysis to identify transcription factor enrichment in the aforementioned driver genes. Two transcription factors, Sp1 and Smad1, emerged as potential regulators of HAM differentiation into SAM (Extended Data Fig. 2h). Immunofluorescence staining using SPP1 and IBA1 antibodies was performed on all four groups, and the number of SPP1+ microglia was quantified (Fig. 3g). In the control group, SPP1+ microglia were significantly more abundant in infarct regions than in non-infarct regions, consistent with previous findings (Fig. 3h). Interestingly, in the infarct region, Slc2a5 knockout mice exhibited significantly higher numbers of SPP1<sup>+</sup> microglia compared to controls, suggesting that *Slc2a5* deficiency promotes the generation of SPP1<sup>+</sup> microglia (Fig. 3h). Furthermore, in non-infarct regions, Slc2a5 knockout mice also displayed a higher number of SPP1+ microglia compared to the control (Fig. 3h). Developmental trajectory analysis using RNA velocity indicated that SAM could differentiate from HAM during AIS. To quantify the extent of differentiation between the two subpopulations, we calculated the ratio of calibrated SAM to HAM numbers and found that this ratio was higher in the Slc2a5 knockout group compared to controls (Fig. 3i). This suggests that Slc2a5 deficiency facilitates the differentiation of microglia into SAM, thereby mitigating brain injury following

To further understand the effects of Slc2a5 deficiency on microglia in infarct and non-infarct regions, we compared the gene expression

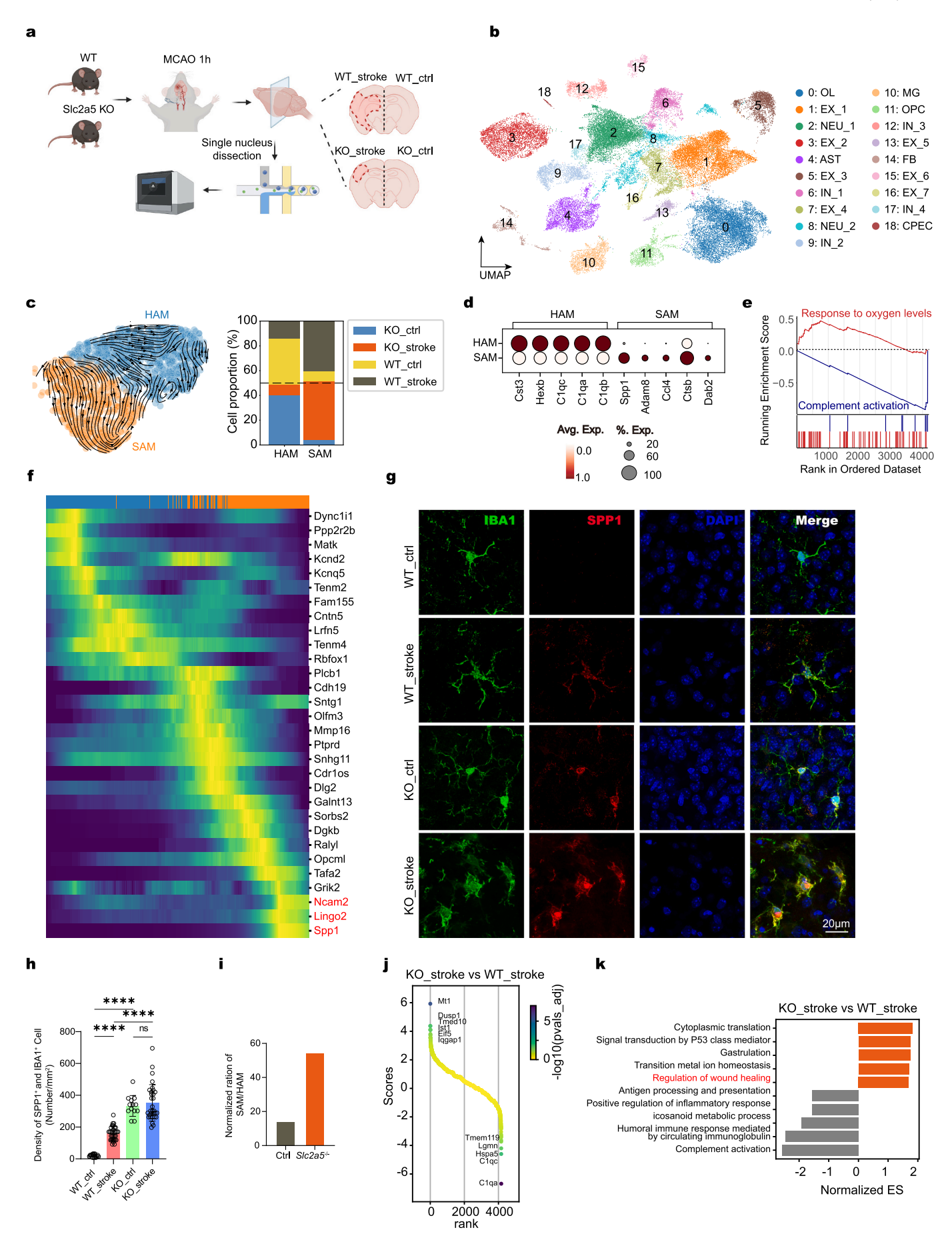


Fig. 3. Slc2a5 deficiency promotes the differentiation of SAM in ischemic stroke

- a. Schema illustrating the development of the single nucleus transcriptome from brain slices of tMCAO in wild-type (WT) and  $Slc2a5^{-/-}$  mice. Wild-type without tMCAO, WT ctrl: Wild-type with tMCAO, WT stroke:  $Slc2a5^{-/-}$  without tMCAO, KO ctrl:  $Slc2a5^{-/-}$  with tMCAO, KO stroke.
- b. UMAP visualization of single nucleus transcriptional profiles from brain slices of tMCAO across various cell types, including oligodendrocyte (OL), excitatory neuron (EX), neuron (NEU), astrocyte (AST), inhibitory neuron (IN), microglia (MG), oligodendrocyte precursor cell (OPC), perivascular fibroblast (FB), and choroid plexus epithelial cell (CPEC).
- c. UMAP visualization featuring RNA velocity streamlines and cell proportions in homeostatic associated microglia (HAM) and stroke associated microglia (SAM), highlighting differences between Slc2a5<sup>-/-</sup> (KO) and wild-type (WT) conditions. Wild-type without tMCAO, WT\_ctrl; Wild-type with tMCAO, WT\_stroke; Slc2a5<sup>-/-</sup> without tMCAO, KO\_ctrl; Slc2a5<sup>-/-</sup> with tMCAO, KO\_stroke.
- d. Dot plot showing the average expression and percentage of expression for marker genes across cell populations in HAM and SAM.
- e. GSEA for the top-ranked genes from SAM (red) and HAM (blue), adjusted p-value <0.05.
- f. Heatmap depicting gene expression patterns under different conditions, illustrating distinct expression profiles associated with HAM and SAM.
- g. Immunofluorescence images displaying IBA1 (green), SPP1 (red), and DAPI (blue) staining in WT and KO mice under control and stroke conditions, with merged images demonstrating colocalization.
- h. Graph quantifying the number of SPP1<sup>+</sup> and IBA1<sup>+</sup> cells in the indicated groups, showing significant differences across conditions (overall p-value <0.0001, \*\*\*\*p < 0.0001). WT\_ctrl, n = 16; WT\_stroke, n = 31; KO\_ctrl, n = 13; KO\_stroke, n = 31. Data are presented as mean ± SEM, with individual data points shown. Statistical significance was determined by one-way ANOVA followed by Tukey's post-hoc testing.
- i. Bar plot of the normalized ratio of SAM vs. HAM in the Ctrl (n = 1) and  $Slc2a5^{-/-}$  (n = 1) groups.
- j. Ranked dot plot comparing KO\_stroke vs. WT\_stroke, revealing differential gene expression patterns.
- k. Bar graphs depicting normalized enrichment scores (ES) for significant pathways altered between KO\_stroke and WT\_stroke, demonstrating the functional impact of genetic changes.

profiles of microglia from these regions in the knockout group and conducted GSEA for pathway enrichment (Fig. 3j, k). Compared to controls, microglia in the infarct region of *Slc2a5* knockout mice showed significant activation of pathways involved in wound healing and tissue repair (Fig. 3k). This indicates that *Slc2a5* deficiency enhances the capacity of microglia in infarct regions to facilitate damage repair following AIS.

#### 3.4. PKM2 mediates the differentiation of SAM in ischemic stroke

To further investigate the effects and underlying mechanisms of Slc2a5 deficiency on microglial differentiation under oxygen-glucose deprivation (OGD), we cultured Slc2a5 knockout microglia in vitro and subjected them to OGD to simulate acute ischemic stroke, subsequently collecting the corresponding microglia for RNA sequencing. Hierarchical clustering results demonstrated significant differences in RNA sequencing among samples, with high data quality (Fig. 4a). First, we compared Slc2a5-deficient microglia to wild-type (WT) microglia under OGD conditions. After 6 h of OGD, Slc2a5-deficient microglia exhibited significant activation of glycolysis pathways and notable changes in the expression of genes related to ATP production (Fig. 4b, d). Additionally, the myeloid immune cell differentiation pathway was significantly activated in Slc2a5-deficient microglia after 6 h of OGD, consistent with previous single-nucleus RNA-seq results showing that Slc2a5 deficiency promotes the differentiation of SPP1+ microglia during acute ischemic stroke (Fig. 4b). Moreover, after 6 h of OGD followed by 24 h of recovery, Slc2a5-deficient microglia showed significant activation of pathways regulating cytotoxicity and suppression of pathways involved in the negative regulation of angiogenesis (Fig. 4c, e). These findings suggest that Slc2a5 deficiency in microglia is beneficial for angiogenesis following acute ischemic stroke. To further explore the unique mechanisms of Slc2a5-deficient microglia under OGD conditions, we compared genes uniquely altered in the OGD and recovery phases. After 6 h of OGD, genes specifically upregulated in Slc2a5deficient microglia were mainly involved in the regulation of myeloid immune cell differentiation (Fig. 4f). Following 6 h of OGD and 24 h of recovery, genes specifically upregulated in Slc2a5-deficient microglia were primarily associated with phagocytosis, indicating that Slc2a5 deficiency enhances the phagocytic ability of microglia in acute ischemic stroke (Fig. 4f).

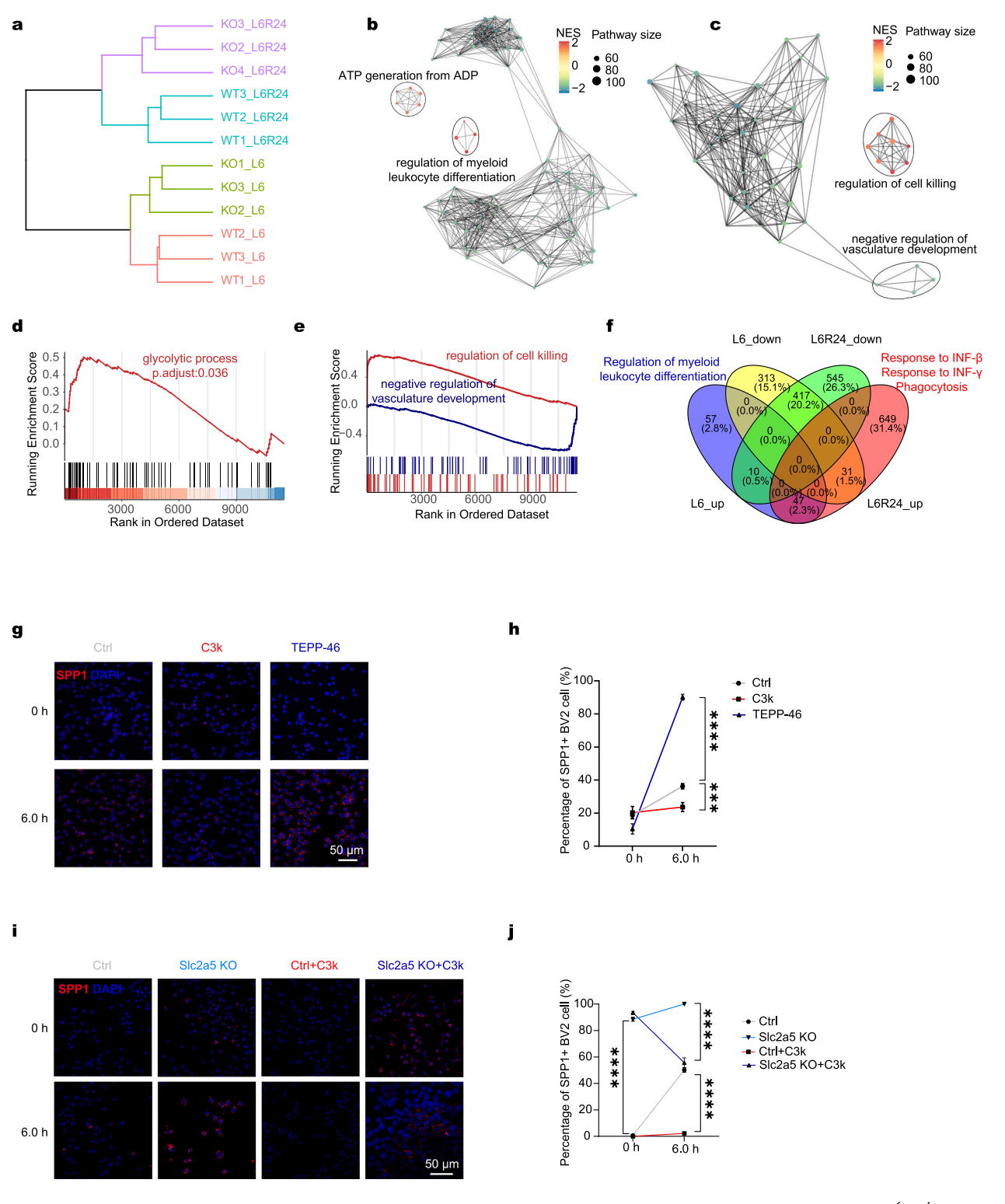
The aforementioned results indicate that the knockout of Slc2a5 in microglia significantly activates the glycolytic pathway under OGD. Previous studies have reported that fructose-1-phosphate, a metabolite derived from Slc2a5-mediated fructose metabolism, directly inhibits

PKM2 [38]. Therefore, we hypothesized that Slc2a5 deficiency may promote microglial differentiation under OGD and treated with PKM2 inhibitors or activators at different time points. Notably, PKM2 activation with TEPP-46 under OGD significantly increased the generation of SPP1<sup>+</sup> BV2 cells, while PKM2 inhibition with C3k significantly decreased the generation of SPP1<sup>+</sup> BV2 cells (Fig. 4g, h). These findings suggest that PKM2 likely mediates the differentiation of microglia during acute ischemic stroke, influencing the production of SAM. To further investigate whether Slc2a5 knockout leads to PKM2 activation, thereby mediating SPP1+ microglia differentiation, we designed an in vitro experiment using BV2 cells with Slc2a5 knockout (Extended Data Fig. 2i) and control groups under OGD, treated with the PKM inhibitor C3k. Results showed that Slc2a5 knockout in BV2 cells exhibited a significantly increased number of SPP1+ cells compared to the control group under normal oxygen conditions (Fig. 4i, j). Simultaneously, PKM2 inhibition significantly reduced the number of SPP1<sup>+</sup> cells under OGD, suggesting that Slc2a5 knockout-induced differentiation of SPP1+ cells is mediated by PKM2 activity (Fig. 4i, j).

# 4. Discussion

Our findings establish microglial *Slc2a5* as a critical regulator of fructose metabolism, orchestrating the transition from homeostatic to SAM and conferring neuroprotection in AIS. This metabolic reprogramming is driven by PKM2 enzymatic activity, linking fructose uptake to microglial functional plasticity. Consistent with pervious reports of elevated brain fructose under neuroinflammatory conditions [39], we demonstrate that blocking Slc2a5-mediated fructose entry—either genetically or pharmacologically—attenuates ischemic injury. While microglia-specific gene deletion provides mechanistic insight, its clinical utility is limited [40], except for cell replacement in microglia [41,42]. Thus, small-molecule SLC2A5 inhibitors may offer a more translatable therapeutic avenue. Our complementary pharmacological experiments suggest that targeting SLC2A5 with small-molecule inhibitors may present a more practical and feasible strategy for therapeutic intervention in AIS.

Single-cell transcriptomic profiling with high-quality control (Extended Data Fig. 3a, b) revealed broad perturbations in microglial subpopulation dynamics following *Slc2a5* deletion under basal conditions. While CCC analysis identified altered signaling networks across brain cell types, the physiological relevance of these baseline alterations remains to be determined. Notably, using single nucleus transcriptomic profiling with high-quality control (Extended Data Fig. 3c, d), we observed a significant expansion of SAM populations—characterized by



(caption on next page)

Fig. 4. PKM2 mediates the differentiation of SAM in ischemic stroke

- a. Hierarchical clustering of samples based on gene expression profiles of microglia from Slc2a5<sup>-/-</sup> (KO) and wild-type (WT) mice. KO and WT samples are grouped and labeled according to treatment conditions L6 and L6R24 (three biological replicates per group): wild-type microglia under OGD for 6 h, WT\_L6; Slc2a5<sup>-/-</sup> microglia under OGD for 6 h, KO\_L6; wild-type microglia under OGD for 6 h followed by 24 h of recovery, WT\_L6R24; Slc2a5<sup>-/-</sup> microglia under OGD for 6 h followed by 24 h of recovery, KO L6R24.
- b. Pathway enrichment network map depicting enriched pathways between KO\_L6 vs. WT\_L6. Node size indicates pathway size, and color represents the Normalized Enrichment Score (NES).
- c. Pathway enrichment network map depicting enriched pathways between KO\_L6R24 vs. WT\_L6R24. Node size indicates pathway size, and color represents the NES.
- d. GSEA plot for the glycolytic process pathway.
- e. GSEA plots showing the enrichment of the regulation of cell killing (red) and negative regulation of vasculature development (blue) pathways.
- f. Venn diagram illustrating shared and unique significant gene sets involved in WT\_L6, KO\_L6, WT\_L6R24, and KO\_L6R24 groups. Down-regulated genes from KO\_L6 vs. WT\_L6, L6\_down; down-regulated genes from KO\_L6R24 vs. WT\_L6R24, L6R24\_down; up-regulated genes from KO\_L6 vs. WT\_L6, L6\_up; up-regulated genes from KO\_L6R24 vs. WT\_L6R24, L6R24 up. Key enriched biological processes are highlighted.
- g. Immunofluorescence images showing SPP1 expression in control and treated samples (C3k, TEPP-46) in BV2 cells with OGD at various time points (0, 6.0 h). Scale bar: 50 µm.
- h. Quantification of SPP1<sup>+</sup> cells over time for Ctrl (n = 5), C3k (n = 5), and TEPP-46 (n = 5). The percentage of SPP1<sup>+</sup> cells is plotted. Statistical significance was determined by two-way ANOVA followed by Tukey's post-hoc testing (\*\*\*\*p < 0.0001, \*\*\*p < 0.0001).
- i. Immunofluorescence images showing SPP1 expression in control and  $Slc2a5^{-/-}$  BV2 cells treated with C3k, with OGD at various time points (0, 6.0 h). Scale bar: 50  $\mu$ m.
- j. Quantification of SPP1<sup>+</sup> cells over time for Ctrl (n = 5), Slc2a5 KO (n = 5), Ctrl + C3k (n = 5), and Slc2a5 KO + C3k (n = 5). The percentage of SPP1<sup>+</sup> cells is plotted. Statistical significance was determined by two-way ANOVA followed by Tukey's post-hoc testing (\*\*\*\*p < 0.0001).

canonical *Spp1* expression [43]—in *Slc2a5*-deficient mice post-AIS, which correlated with improved neuropathological outcomes. RNA velocity trajectories and transcription factor (TF) enrichment implicated *Sp1* and *Smad1* in SAM differentiation; however, the precise regulatory interplay between SLC2A5 inhibition and these TFs requires further elucidation.

Research has demonstrated that fructose-1-phosphate, a unique metabolite in the fructose metabolism pathway, inhibits PKM2 protein activity [38]. By inhibiting PKM2 protein activity in BV2 cells during OGD, we found that this inhibition prevented the production of SPP1<sup>+</sup> cells(Fig. 4i, j). This finding supports the idea that blocking SLC2A5 reduces fructose-1-phosphate levels, increases PKM2 activity, and consequently promotes SPP1<sup>+</sup> microglial polarization. However, the absence of clear cytotoxicity or proliferation controls in our OGD model limits the interpretability of these polarization data. Emerging evidence suggests PKM2 regulates inflammatory responses via lactate-driven histone lactylation [44,45]. While our data establish SLC2A5-PKM2 signaling as critical for SAM differentiation, future studies must address whether this pathway modulates lactylation dynamics at the Sp1/Smad1 promoter regions during AIS.

Transcriptomic analysis revealed enhanced phagocytic gene signatures in *Slc2a5*-deficient microglia after hypoxia. This suggests, albeit with limited statistical power, that accelerated debris clearance contributes to neuroprotection. Intriguingly, *Slc2a5* ablation induced rapid M2-like polarization within 24 h post-AIS (Fig. 4f)—a temporal window substantially narrower than the canonical 72-h neuroinflammatory timeline [46]. This accelerated phenotypic switching highlights SLC2A5 inhibition as a potential strategy to amplify microglial phagocytic responses during early stroke pathogenesis.

Emerging evidence has documented the presence of SPP1<sup>+</sup> microglia across multiple neuropathological conditions, particularly in gliomas, amyotrophic lateral sclerosis (ALS), Alzheimer's disease (AD), and multiple sclerosis (MS) [43]. However, the mechanistic underpinnings and functional significance of this microglial subpopulation remain elusive. While previous work established that genetic ablation of *Slc2a5* significantly impairs tumor progression in experimental glioma models [47]. Our current investigation reveals that inhibiting SLC2A5 leads to an increase in SPP1<sup>+</sup> microglial accumulation under AIS, resulting in a protective effect. Mechanistically, pharmacological blockade of SLC2A5 depletes intracellular fructose-1-phosphate pools, diminishing its suppressive effect on PKM2 activity. This metabolic reprogramming promotes the hypoxic differentiation of SPP1<sup>+</sup> microglia through enhanced PKM2-mediated glycolytic flux. Our findings establish a targeted methodology for modulating microglial polarization states in disease

microenvironments, facilitating systematic investigation of SPP1<sup>+</sup> microglial functions in neurological pathogenesis.

#### 5. Conclusion

Collectively, our study has, for the first time, revealed the neuroprotective mechanism and role of SLC2A5 following AIS. This gene primarily regulates the differentiation of SPP1<sup>+</sup> microglia through the PKM2 pathway. As a gene that is specifically and highly expressed in central nervous system microglia, SLC2A5 shows significant potential as a target for regulating microglial states and holds valuable translational therapeutic applications for acute ischemic stroke and other brain diseases.

Supplementary data to this article can be found online at https://doi. org/10.1016/j.metabol.2025.156429.

# CRediT authorship contribution statement

Daosheng Ai: Writing – original draft, Methodology, Investigation. Baoshan Qiu: Visualization, Methodology, Data curation. Xing-jun Chen: Methodology, Data curation. Fengzhi Li: Methodology, Data curation. Di Yao: Methodology. Huijie Mi: Methodology. Jun-Liszt Li: Methodology. Bing Zhou: Writing – review & editing. Jian Zuo: Resources. Yilong Wang: Writing – review & editing, Methodology. Wooping Ge: Writing – review & editing, Funding acquisition, Conceptualization. Wenzhi Sun: Writing – review & editing, Supervision, Funding acquisition, Conceptualization.

#### **Declaration of competing interest**

All authors have no competing interests.

# Acknowledgement

We thank all members of Sun lab and Ge lab at the Chinese Institute for Brain Research (CIBR), Beijing. This work was supported by grants from the STI2030-Major Projects (2022ZD0204700 to W. S. and W.G.), CAMS Innovation Fund for Medical Sciences (CIFMS, 2024-I2M-ZD-012 to W.G.), the Natural Science Foundation of China (No. 32170964 to W. G.), Youth Beijing Scholar Program (No. 065 to W.G.), and Startup Funds from CIBR to W. S. and W.G..

#### Data availability

All related scripts can be found at <a href="https://github.com/Sunwenzhilab/Slc2a5\_Ai">https://github.com/Sunwenzhilab/Slc2a5\_Ai</a>. All data are available in the main text or the supplementary materials; sequencing data have been deposited in the NCBI GEO under accession numbers GSE289791 and GSE289792.

#### References

- [1] Feigin VL, et al. Global, regional, and national burden of stroke and its risk factors, 1990–2021: a systematic analysis for the global Burden of disease study 2021. Lancet Neurol. 2024;23:973–1003.
- [2] Vos T, et al. Global burden of 369 diseases and injuries in 204 countries and territories, 1990–2019: a systematic analysis for the global Burden of disease study 2019. Lancet. 2020;396:1204–22.
- [3] Zhu W, et al. Global and Regional Burden of Ischemic Stroke Disease from 1990 To 2021: An age-period-cohort analysis. Transl Stroke Res. 2025;16(5):1474–85.
- [4] Paul S, Candelario-Jalil E. Emerging neuroprotective strategies for the treatment of ischemic stroke: an overview of clinical and preclinical studies. Exp Neurol. 2021; 335:113518.
- [5] Alsbrook DL, et al. Neuroinflammation in acute ischemic and hemorrhagic stroke. Curr Neurol Neurosci Rep. 2023;23:407–31.
- [6] Prinz M, Masuda T, Wheeler MA, Quintana FJ. Microglia and Central Nervous System–Associated Macrophages—From Origin to Disease Modulation. Annu Rev Immunol. 2021;39:251–77.
- [7] Qin C, et al. Dual functions of microglia in ischemic stroke. Neurosci Bull. 2019;35: 921–33
- [8] Jin W-N, et al. Depletion of microglia exacerbates postischemic inflammation and brain injury. J Cereb Blood Flow Metab. 2017;37:2224–36.
- [9] Hu Y, et al. Dual roles of hexokinase 2 in shaping microglial function by gating glycolytic flux and mitochondrial activity. Nat Metab. 2022;4:1756–74.
- [10] Ma W-Y, et al. A breakdown of metabolic reprogramming in microglia induced by CKLF1 exacerbates immune tolerance in ischemic stroke. J Neuroinflammation. 2023-20-97
- [11] Harrell CS, et al. High-fructose diet during adolescent development increases neuroinflammation and depressive-like behavior without exacerbating outcomes after stroke. Brain Behav Immun. 2018;73:340–51.
- [12] Jung S, Bae H, Song W-S, Jang C. Dietary fructose and fructose-induced pathologies. Annu Rev Nutr. 2022;42:45–66.
- [13] Park S-H, et al. Fructose induced KHK-C can increase ER stress independent of its effect on lipogenesis to drive liver disease in diet-induced and genetic models of NAFLD. Metab Clin Exp. 2023;145.
- [14] Tobey TA, Mondon CE, Zavaroni I, Reaven GM. Mechanism of insulin resistance in fructose-fed rats. Metab Clin Exp. 1982;31:608–12.
- [15] Spagnuolo MS, Iossa S, Cigliano L. Sweet but bitter: focus on fructose impact on brain function in rodent models. Nutrients. 2020;13:1.
- [16] Herman MA, Birnbaum MJ. Molecular aspects of fructose metabolism and metabolic disease. Cell Metab. 2021;33:2329–54.
- [17] Zhang Y, et al. An RNA-sequencing transcriptome and splicing database of glia, neurons, and vascular cells of the cerebral cortex. J Neurosci. 2014;34:11929–47.
- [18] Wu X, et al. Glucose transporter 5 is undetectable in outer hair cells and does not contribute to cochlear amplification. Brain Res. 2008;1210:20–8.
- [19] Kaiser T, Feng G. Tmem119-EGFP and Tmem119-CreERT2 transgenic mice for labeling and manipulating microglia. eNeuro. 2019;6(4). ENEURO.0448-18.
- [20] Jia J-M, et al. Control of cerebral ischemia with magnetic nanoparticles. Nat Methods. 2017;14:160–6.
- [21] Qiu B, et al. A systematic observation of vasodynamics from different segments along the cerebral vasculature in the penumbra zone of awake mice following cerebral ischemia and recanalization. J Cereb Blood Flow Metab. 2023;43:665–79.

- [22] Reglodi D, et al. Effects of pretreatment with PACAP on the infarct size and functional outcome in rat permanent focal cerebral ischemia. Peptides. 2002;23: 2227–34.
- [23] Gao X, et al. Reduction of neuronal activity mediated by blood-vessel regression in the adult brain. Nat Commun. 2025;16:5840.
- [24] Li F, et al. Morroniside protects OLN-93 cells against H2O2-induced injury through the PI3K/Akt pathway-mediated antioxidative stress and antiapoptotic activities. Cell Cycle. 2021;20:661–75.
- [25] Kim D, Paggi JM, Park C, Bennett C, Salzberg SL. Graph-based genome alignment and genotyping with HISAT2 and HISAT-genotype. Nat Biotechnol. 2019;37: 907-15.
- [26] Liao Y, Smyth GK, Shi W. featureCounts: an efficient general purpose program for assigning sequence reads to genomic features. Bioinformatics. 2014;30:923–30.
- [27] Love MI, Huber W, Anders S. Moderated estimation of fold change and dispersion for RNA-seq data with DESeq2. Genome Biol. 2014;15:550.
- [28] Yu G, Wang L-G, Han Y, He Q-Y. clusterProfiler: an R package for comparing biological themes among gene clusters. OMICS. 2012;16:284–7.
- [29] Ai D, et al. Transcriptomic profiling unveils EDN3+ meningeal fibroblasts as key players in Sturge-weber syndrome pathogenesis. Adv Sci. 2025;12:2408888.
- [30] Wolf FA, Angerer P, Theis FJ. SCANPY: large-scale single-cell gene expression data analysis. Genome Biol. 2018;19:15.
- [31] Korsunsky I, et al. Fast, sensitive and accurate integration of single-cell data with harmony. Nat Methods. 2019;16:1289–96.
- [32] Fang Z, Liu X, Peltz G. GSEApy: a comprehensive package for performing gene set enrichment analysis in Python. Bioinformatics. 2023;39.
- [33] Jin S, et al. Inference and analysis of cell-cell communication using CellChat. Nat Commun. 2021;12:1088.
- [34] Dong X-H, Sun X, Jiang G-J, Chen AF, Xie H-H. Dietary intake of sugar substitutes aggravates cerebral ischemic injury and impairs endothelial progenitor cells in mice. Stroke. 2015;46:1714–8.
- [35] Funari VA, Crandall JE, Tolan DR. Fructose metabolism in the cerebellum. Cerebellum. 2007;6:130–40.
- [36] Raffaele S, et al. Microglial TNFR2 signaling regulates the inflammatory response after CNS injury in a sex-specific fashion. Brain Behav Immun. 2024;116:269–85.
- [37] Bergen V, Lange M, Peidli S, Wolf FA, Theis FJ. Generalizing RNA velocity to transient cell states through dynamical modeling. Nat Biotechnol. 2020;38: 1408–14.
- [38] Taylor SR, et al. Dietary fructose improves intestinal cell survival and nutrient absorption. Nature. 2021;597:263–7.
- [39] Chen Q, et al. Metabolomics profiling to characterize cerebral ischemia-reperfusion injury in mice. Front Pharmacol. 2023;14:1091616.
- [40] Wen Y, et al. Kdm6a deficiency in microglia/macrophages epigenetically silences Lcn2 expression and reduces photoreceptor dysfunction in diabetic retinopathy. Metab Clin Exp. 2022;136.
- [41] Xu Z, et al. Efficient strategies for microglia replacement in the central nervous system. Cell Rep. 2020;32:108041.
- [42] Wu J, et al. Microglia replacement halts the progression of microgliopathy in mice and humans. Science. 2025;389:eadr1015.
- [43] Lan Y, et al. Fate mapping of Spp1 expression reveals age-dependent plasticity of disease-associated microglia-like cells after brain injury. Immunity. 2024;57: 349–363.e9.
- [44] Pan R-Y, et al. Positive feedback regulation of microglial glucose metabolism by histone H4 lysine 12 lactylation in Alzheimer's disease. Cell Metab. 2022;34: 634–648.e6.
- [45] Chen C, et al. Lactylation as a metabolic epigenetic modification: mechanistic insights and regulatory pathways from cells to organs and diseases. Metab Clin Exp. 2025;169.
- [46] Gao X, et al. Research progress on mechanisms of ischemic stroke: regulatory pathways involving microglia. Neurochem Int. 2024;172:105656.
- [47] Chen C, et al. ATF4-dependent fructolysis fuels growth of glioblastoma multiforme. Nat Commun. 2022;13:6108.